doi.org/10.15407/tpwj2016.04.02

INFLUENCE OF ELECTRIC-MAGNETIC COMPOSITE FIELD ON WC PARTICLES DISTRIBUTION IN LASER MELT INJECTION*

LIANG WANG[1, 2], **YONG HU**[1, 2], **SHIYING SONG**[1, 2] and **JIANHUA YAO**[1, 2]
[1]Research Center of Laser Processing Technology and Engineering, Zhejiang University of Technology
18 Chaowang Str., 310014, Hangzhou, PRC. E-mail: ddtwl@foxmail.com
[2]Zhejiang Provincial Collaborative Innovation Center of High-end Laser Manufacturing Equipment
Hangzhou, PRC

The laser melt injection (LMI) method is always used to prepare a metal-matrix composite layer on the surface of substrate. In LMI process, the laser beam melts the surface layer of substrate locally while simultaneously injecting particles of additional material. In order to control the distribution of reinforcement particles in LMI layer, an electric-magnetic composite field can be applied. The effect of electric-magnetic synergistic on the reinforcement particles distribution in LMI was investigated using experimental and numerical method. The spherical WC particles were used because their regular shape was most close to the simulation conditions and good tracer performance in the melt flow. The distribution of WC particles in longitudinal section was observed by SEM and calculated by computer graphics processing. The trajectory of WC particles in the melt pool was simulated by a 2D model coupled the equations of heat transfer, fluid dynamics, drag force, Lorentz force and phase transition. The simulation results were compared with experimental data and were in good agreement. The results indicated that the effect of electric-magnetic synergistic on the reinforcement particles distribution was verified. The distribution of WC particles in LMI-layer was influenced by the direction of Lorentz force induced by electric-magnetic composite field. When the Lorentz force and gravity force are in the same direction, the vast majority of particles are trapped in the upper region of LMI-layer, and when these forces are in the opposite direction, most particles are concentrated in the lower region. 34 Ref., 8 Figures.

Keywords: *laser melt injection, WC particles, Lorentz force, particles distribution, electric-magnetic composite field*

Metal-matrix composites (MMC) reinforced with ceramic particles exhibit a number of advantages over monolithic alloys and have been used extensively in industry [1]. The laser melt injection (LMI) method is always used to prepare a MMC layer on the surface of substrate with low particle dissolution rate, high surface performance and low cracking tendency [2–5]. LMI has been mainly applied for improving the surface hardness and wear resistance of the metallic substrate, such as stainless steels [4, 6], aluminum alloys [7, 8], titanium alloys [1, 2, 9–11], low carbon steels [12–16] and tool steels [3, 5, 17]. In contrast with laser cladding, the reinforcement particles (usually ceramics) injected in the molten pool without any other metal-matrix powder and moved with the melt flow preserve solid state or micromelt state due to rapid solidification during LMI process [7].

Graded materials can be designed at microstructural level to tailor specific materials for their functional performance in particular applications [18, 19]. The controlled gradients in mechanical properties offer attractive challenges for the design of surfaces with resistance to contact deformation and damage [9]. In order to optimize the particle utilization ratio, machinable property and gradient distribution performance of LMI-layers, it is necessary to control the distribution of reinforcement particles. The previous LMI process usually chose the special designed lateral nozzle as a powder delivery nozzle for avoiding the excessive dissolution of reinforcement particles [16]. Therefore, the injection angle with respect to the surface normal [20], relative position between the powder spot and laser spot [21] and powder injection velocityy [7, 22] are the key process parameters during powder injection, which influence the distribution status of reinforcement particles sensitively. Consequently, it is difficult and time-consuming to adjust the distribution of reinforcement particles because the processing parameters window of LMI using lateral nozzle powder delivery system is very narrow [6, 7].

*Based on materials presented at Seventh International Conference «Laser technologies in welding and materials processing», September 14–18, 2015, Odessa, Ukraine.

In this research, a common coaxial nozzle was chose to replace the special designed lateral nozzle to simplify the adjusting process of powder delivery system. However, both the injection angle with respect to the surface normal and the relative position between the powder spot and laser spot are fixed during coaxial LMI process. In order to control the distribution of WC particles using coaxial nozzle, an external force was introduced during LMI process, which applies an electric-magnetic composite field (EMCF) to the melt pool.

The application of electromagnetic field is a positive practice in laser welding and laser alloying to influence the distribution of added elements. Effect of electromagnetic stirring on the element distribution in laser welding was investigated by numerical and experimental methods. It was shown that the change of distribution of the filler material results from modulation of the melt flow due to periodic induced electromagnetic volume forces [23]. The frequency is a main parameter to determine the spatial distribution of elements, whereas the magnetic flux density is the main parameter determining the overall scale of the magnetic manipulation [24, 25].

A numerical model is built to investigate the laser-melted aluminum pool under the influence of static magnetic field. The solute distribution in the solid depends on the applied magnetic induction [26]. The other effects of electromagnetic field include suppressing surface undulation of laser remelting, damping the velocity of molten pool [27], reducing the defects of laser welding [28, 29], preventing gravity dropout of the melt during laser full-penetration welding [30 et al.].

The previous investigations in electromagnetic fields were mostly focused on the influences of the elements, temperature, velocity and defects distribution on the melt pool during laser processing, all of which are induced through AC magnetic field or melt flow in the steady magnetic field. In this work, both the external steady electric field and the steady magnetic field were added in the molten pool during LMI process synchronously. The Lorentz force, generated by the electric-magnetic synergistic effect, is a kind of directional volume force in the melt pool in LMI, similar to gravity. This Lorentz force can function as an additional volume force acting on the melt flow with variable direction. Consequently, the positions of WC particles trapped in the molten pool will be changed without changing LMI parameters.

In this research, a 2D transient multi-physics numerical model, concerning heat transfer, fluid dynamics, phase transition, drag force acted on the particles and electromagnetic field, was employed to study the distribution mechanism of reinforcement particles during LMI under the EMCF. The partial differential equations were solved with the finite-element solver COMSOL Multiphysics. The simulation results were verified by experimental measurements.

Experimental methods. AISI 316L austenitic stainless steel was used as the substrate because of its paramagnetic property. The chemical composition of AISI 316L was as follows, wt.%: 0.02C, 0.55Si, 1.55Mn, 0.03P, 0.03S, 10Ni, 16.5Cr, 2.08Mo, Fe — base. Spherical monocrystalline WC particles (without W_2C) were chosen as the reinforcement particles, because the particles of this shape were used in the simulation study due to their good tracing performance in the melt flow. The size of WC particles was 75–150 μm (Figure 1). The substrate specimens were machined to long strips with dimensions of 200×20×10 mm. Figure 2 shows the schematic diagram of the LMI process with EMCF applied. The electromagnets were used to provide the steady magnetic field (maximum magnetic flux density is 2 T), and large-capacity lead-acid batteries (2 V, 500 A·h) were used to provide high current (steady electric field) for the melt pool. In the melt pool zone, the magnetic flux density was of about 0.4–2.0 T, and the average current density — of about 5 A/mm^2.

LMI was conducted using the 2 kW diode laser LASERLINE, powder feeder and coaxial nozzle. Argon was used as a shielding gas to reduce oxidation of the specimen and WC particles. Laser beam diam-

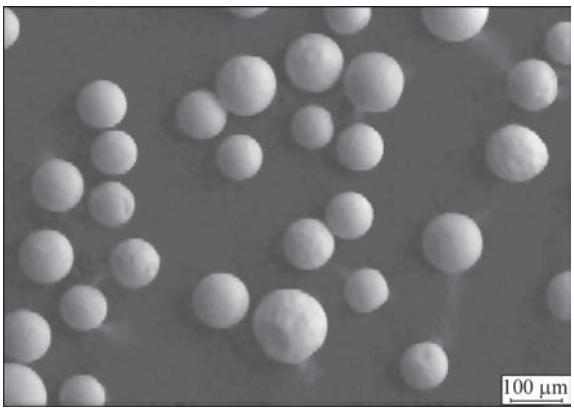

Figure 1. SEM-image of spherical monocrystalline WC particles used

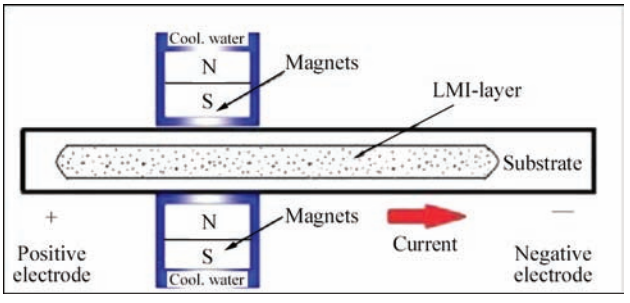

Figure 2. Schematic of LMI process with EMCF

eter, optimized laser power, scanning speed and powder feed rate in this experiment were 4 mm, 1.6 kW, 5 mm/s and 10 g/min, respectively. The distribution of WC particles and elements in the melt pool were observed using SEM (Carl Zeiss SIGMA HV-01-043) and EDS (Bruker Nano X-Flash Detector 5010). The gradient distribution of microhardness *HV* was test by the microhardness tester (Shimadzu HMV-FA2).

Numerical simulation. *Governing equations.* The numerical simulation of the LMI process involves a classical computational fluid dynamics approach, that concerns fluid flow field and pressure as well as temperature. The movement of injected particles was calculated by the Lagrangian approach with fluid–particle coupling [18, 19]. The influence of Lorentz force induced by EMCF was added in the source term of momentum equations as the volume force. The computational domain was initially composed of 30×5 mm rectangle. The surrounding gas phase was not taken into account because of the large differences in density and dynamic viscosity between the liquid metal and gas phase. The basic assumptions, made on the fluid flow, temperature field, particles injection and electromagnetic field in the simulation, were as follows:

- laminar flow pattern is assumed. The main reason for this choice is that the velocities outside the shear layers at the surfaces are significantly reduced, and the Reynolds number inside the molten pool turn out to be far less than turbulent critical value (10^3) [30]. Furthermore, laminar flow assumption makes the numerical solution easier and reduces the computational effort [31];
- material properties are temperature-dependent up to evaporation temperature;
- Joule heat induced by high current is neglected due to short action time and strong laser heating of the metal up to evaporation temperature;
- buoyancy of molten pool is determined using Boissinesq approximation, because density variation caused by the temperature difference is sufficiently small;
- thermal conductivity is adjusted properly according to the actual situation, since the convective motion in the transverse plane (*z*-direction) is neglected in 2D models, that may result in heat redistribution due to the fluid flow [32];
- distribution of magnetic flux density in the active area is uniform;
- injection direction of particles is perpendicular to the substrate of molten pool, and particles are spherical and uniformly distributed in the powder jet;
- in the LMI process, the injecting particles maintain non-melting state, and their shape is spherical regularly. Therefore, the drag force (Stoke's force) acting on the particles is only related to the velocity of melt flow [7];
- heat and convection in the molten pool are not influenced by the injection of particles;
- effect of gravity and drag exerted by the surrounding gas on particle movement are negligible, and all particles have the same velocity.

The governing equations for mass conservation, energy conservation, momentum conservation including Darcy force and Lorentz force are solved using the finite-element package COMSOL Multiphysics.

Mass conservation is expressed as

$$\nabla(\rho u) = 0, \tag{1}$$

and momentum conservation is given as

$$\rho\frac{\partial u}{\partial t} + \rho(u\nabla)u = \nabla[-pI + \eta(\nabla u + (\nabla u)^T)] + \\ + F_{\text{Buoyancy}} + F_{\text{Darcy}} + F_{\text{Lorentz}}, \tag{2}$$

where ρ is the density; p is the pressure; η is the viscosity; F_{Buoyancy}, F_{Darcy} and F_{Lorentz} are the source terms, represent the buoyancy force, Darcy force, and Lorentz force, respectively. The buoyancy force comes from density gradients, which is related to the expansion of the liquid metal and is usually expressed using the Boissinesq approximation as follows:

$$F_{\text{Buoyancy}} = \rho(1 - \beta(T - T_{\text{m}}))g, \tag{3}$$

where β is the thermal expansion coefficient; g is the gravivational constant; T is the temperature; and T_{m} is the melting point.

The role of Darcy term is to dampen the velocity at the phase interface, therefore it becomes the velocity of solidified phase after transition. This term is assumed to vary with the liquid fraction and can be expressed according to the Kozeny–Carman equation [33] as

$$F_{\text{Darcy}} = -A_{\text{mush}}\frac{(1 - f_{\text{l}})^2}{f_{\text{l}}^3 + c}u, \tag{4}$$

where F_{l} is the volume fraction of the liquid phase, A_{mush} and c are the arbitrary constants (A_{mush} should be a large-valued constant accounting for damping the velocity of the mushy region, and c is the small constant to avoid division by zero in the solid region).

The liquid fraction f_{l} is assumed to vary linearly with temperature in the mushy zone, which is delimited by the solidus T_S and liquidus T_L temperatures. It is defined as

$$f_{\text{L}} = \begin{cases} 0 & T < T_S, \\ \dfrac{T - T_{\text{S}}}{T_L - T_S} & T_S \le T \le T_L, \\ 1 & T > T_L. \end{cases} \tag{5}$$

The Lorentz force F_{Lorentz} induced by the external steady magnetic field, steady electric field and conductive fluid motion is described by the following equation:

$$F_{\text{Lorenz}} = jB = \sigma(E + uB) \times \\ \times B = \sigma(EB + uB^2), \quad (6)$$

where j is the current density; B is the magnetic flux intensity; E is the external electric field; and σ is the electric conductivity.

The interaction of external magnetic field with external electric field builds up the directional Lorentz force contribution (σ(EB)). Simultaneously, the movement of conducting melt flow in the external magnetic field generates the induced electric current. This induced current in the same external magnetic field forms the nondirectional Lorentz force (σ(μB^2)), which has a component directed against the original melt velocity thus decelerating the melt.

Energy conservation is given as

$$\rho C_p \frac{\partial T}{\partial t} + \rho C_p u \nabla T = \nabla (k \nabla T) + Q_{\text{source}}, \quad (7)$$

where C_p is the heat capacity; k is the thermal conductivity; and Q_{source} is the heat source from laser beam.

The movement of particles in the molten pool obeys Newton's second law:

$$\frac{d(m_p v)}{dt} = F_D + F_g + F_{\text{Buoyancy}}; \quad (8)$$

$$F_D = m_p \left(\frac{1}{\tau_p} \right) (u - v); \quad (9)$$

$$F_g = m_p g; \quad (10)$$

$$F_{\text{Buoyancy}} = V_p \rho_f g, \quad (11)$$

where m_p is the particle mass; F_D is the drag force; F_g is the gravity; u is the fluid velocity; v is the particle velocity; g is gravity acceleration; V_p is the volume of one particle; and ρ_f is the fluid density.

The relative Reynolds number is Re_r = 1–100, and the drag coefficient based on Schiller–Naumann drag mode is calculated as follows:

$$\text{Re}_r = \frac{\rho_f |u - v| d_p}{\mu}; \quad (12)$$

$$C_D = \frac{24}{\text{Re}_r} \left(1 + 0.15 \text{Re}_r^{0.637} \right); \quad (13)$$

$$\tau_p = \frac{4 \rho_p d_p^2}{3 \mu C_D \text{Re}_r}, \quad (14)$$

where d_p is the diameter of particle; μ is the dynamic viscosity; and ρ_p is the particle density.

Boundary conditions. The temperature of the substrate is assumed to be the same as ambient temperature T_0 initially. The energy distribution of laser beam is considered uniform because of the nature of diode laser. Surface tension is added on the top surface as the boundary condition, which is relevant to the surface temperature of molten pool. In this model, surface tension is expressed by Marangoni shear stresses using the test function of the computation software:

$$-\eta \frac{\partial u}{\partial z} = \frac{\partial \gamma}{\partial T} \frac{\partial T}{\partial x}, \quad -\eta \frac{\partial \upsilon}{\partial z} = \frac{\partial \gamma}{\partial T} \frac{\partial T}{\partial y}, \quad (15)$$

where η is the viscosity; $\partial\gamma/\partial T$ is the temperature derivative of the surface tension.

The injection velocity of the WC particles is calculated as follows [34]:

$$u = \frac{3 D^2 v_0^2}{32 \upsilon} \frac{\cos \theta}{R}, \quad (16)$$

where D is the nozzle hydraulic diameter; v_0 is the carrier gas velocity at the nozzle; υ is the kinematic viscosity; θ is divergence angle of particle; and R is the distance between nozzle and sample. The particle injection velocity was calculated about 1.1 m/s and powder spot center was coincided with laser spot center.

Boundary conditions of numerical model are illustrated in Figure 3. The necessary velocity and heat bounrady conditions were as follows:

- top boundary: $-\eta u_{i,k} = \frac{\partial \gamma}{\partial T} \frac{\partial T}{\partial x_i} (i = 1, 2; k = 3)$; $q_0 = h(T_{\text{ext}} - T)$;
- left boundary: $u\mathbf{n} = 0$; $q_0 = h(T_{\text{ext}} - T)$;
- bottom boundary: $u\mathbf{n} = 0$; $-\mathbf{n}(-k\nabla T) = 0$;
- right boundary: $u\mathbf{n} = 0$; $q_0 = h(T_{\text{ext}} - T)$.

The melting temperature of material was 1700 K; fluid density 7800 kg·m^{-3}; particles density 15600 kg·m^{-3}; heat capacity 746 J·kg^{-1}·K^{-1}; latent heat of fusion 30 J·kg^{-1}; heat conductivity 30 W·m^{-1}·K^{-1}; dynamic viscosity 0.006 Pa·s; surface tension coeffi-

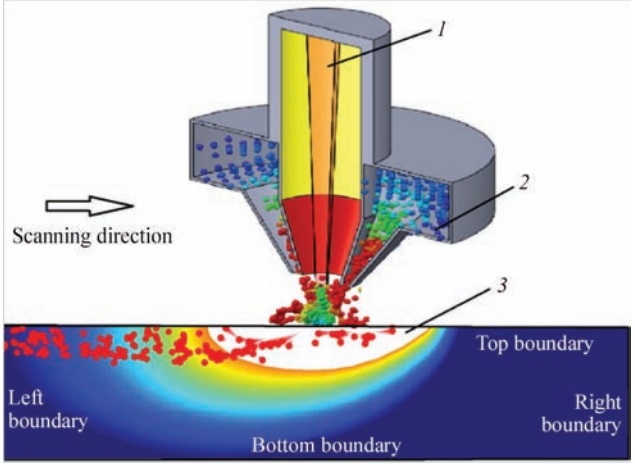

Figure 3. Boundary conditions of numerical model: *1* — laser beam; *2* — particles; *3* — molten pool

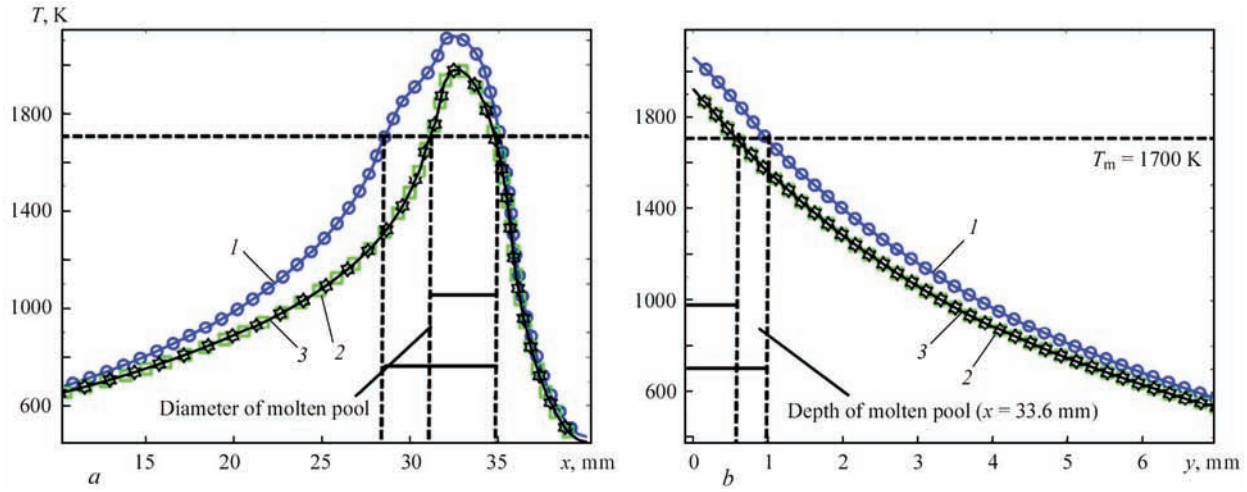

Figure 4. Temperature distribution along the surface (*a*) and along the depth (*b*) of molten pool: *1* — B = 0; *2* — 0.6; *3* — 1.2 T

cient $–0.52·10^{–4}$ N·m$^{–1}$·K$^{–1}$; diameter of particles was 80 μm. The processing parameters were as follows: diameter of laser spot of 4 mm; laser scanning speed of 4 mm·s$^{–1}$; laser power of 1700 W; powder feed rate of 15 g·min$^{–1}$; shielding gas flow rate of 10 l·min$^{–1}$.

Results and discussion. *Temperature and velocity distribution.* The temperature distribution along the surface of molten pool (x-direction, y = 0 mm) is plotted in Figure 4, *a*, and along its depth at the center of laser spot (y-direction, x = 33.6 mm) — in Figure 4, *b*. It is seen that the high temperature zone of the molten pool with Lorentz force are suppressed. No matter the Lorentz force is upward or downward, the temperature distribution with EMCF is always lower than that without it. In contrast with temperature distribution, the fluid velocity distribution is influenced by EMCF more significantly. Figure 5, *a* shows the velocity distribution along the surface, and Figure 5, *b* — the depth of molten pool. The maximum fluid velocity of molten pool is about 0.08 mm/s without EMCF. With the influence of the directional Lorentz force induced by EMCF, the maximum fluid velocity of molten pool is decreased to less than 0.02 mm/s, whether the direction of Lorentz force is upward or downward. The double peaks of velocity distribution depict the difference in maximum velocity because of the heat accumulation effect and Marangoni effect during laser remelting process. On each side of the peak temperature location, thermal gradients are of opposite sign, leading to fluid flow velocity equal to zero at that point due to Marangoni effect. The thermal gradients become maximal at the edge of laser beam, that explains the velocity peaks observed [32].

Particles distribution. Figure 6, *a*, *b* shows the longitudinal sections of the LMI-layers with particle distribution prepared with different directions of Lorentz force induced by EMCF. Figure 6, *c* shows the longitudinal section of the LMI-layer prepared without external Lorentz force. Due to the same LMI process parameters conducted, the thickness of the LMI-layers and the fraction of injected particles in the LMI-layer are almost the same for the three specimens. In order to investigate the quantitative difference of particles between the three distributions, all the LMI-layers were divided into two regions (upper

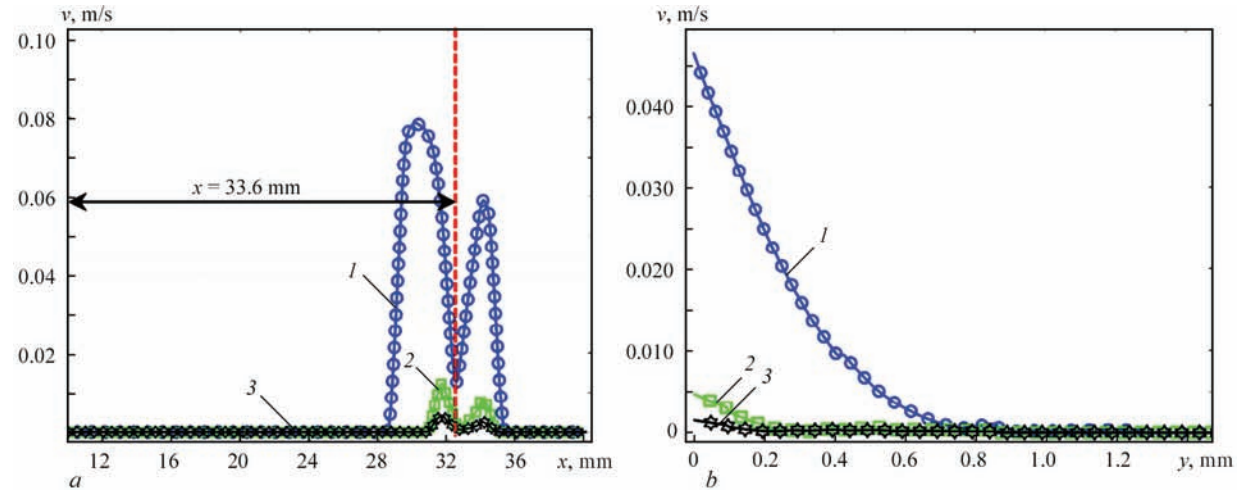

Figure 5. Velocity distribution along the surface (*a*) and along the depth (*b*) of molten pool : *1* — B = 0; *2* — 0.6; *3* — 1.2 T

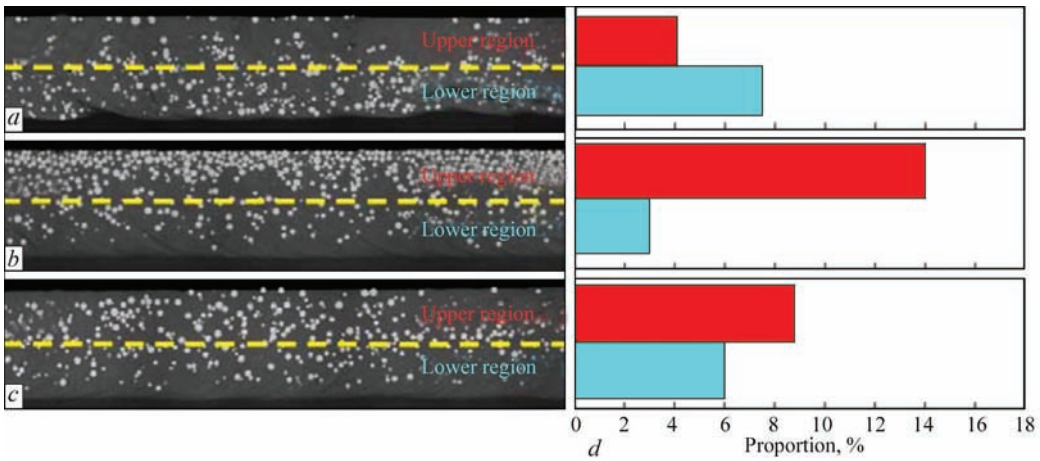

Figure 6. Distributions of WC particles in the longitudinal sections of LMI-layers at upward (*a*) and downward (*b*) direction of Lorentz force and without (*c*) external Lorentz force, and proportion of WC particles in upper and lower regions (*d*)

and lower) equally. The proportions of WC particles in both regions were computed via computer graphics processing. The calculating results are attached to the corresponding LMI-layers in Figure 6, *d*.

Under the upward Lorentz force, most particles are concentrated in the lower region. The proportion in the lower region is more than 50 % of that in the upper region. Only a small number of WC particles were trapped in the near-surface of LMI-layer. Contrarily, the majority of particles are trapped in the upper region when the direction of Lorentz force is downward (see Figure 6, *b*). The particles could hardly be sunken into the lower region of molten pool. The particles are distributed uniformly in the LMI-layer produced without EMCF applied (see Figure 6, *c*). The Lorentz force generated by the steady magnetic and electric field is a kind of directional steady volume force in the melt pool. The direction of the Lorentz force acting on the fluid is in the opposite direction of the corresponding force acting on the particles. Taking into consideration equations (1) and (2).

$$F_{\cdot} = (jB)V, \tag{17}$$

where V is the volume of fluid displaced by one particle, and

$$F_{\mathrm{L}} = -\mathrm{L}_{\mathrm{p}}, \tag{18}$$

where L_{p} is the counteracting Lorentz force acting on the particle. Because the WC particles are non-conducting and non-magnetic, the Lorentz force does not act on the particle directly.

Diagram of the forces acting on one particle and surrounding fluid is shown in Figure 7. When the Lorentz force acting on the fluid is assumed as upward, the following balance equation is established to express the force (in *y*-direction) acting on the particle:

$$-F_{iy} = F_{\mathrm{B}} - {}_{\mathrm{p}} + F_{dy} - G_{\mathrm{p}} \tag{19}$$

where F_{iy}, F_{dy} and G_{p} are the inertia force, drag force and gravity, respectively. F_{B}, F_{dy} and G_{p} are assumed to be constant, thus, F_{iy} and L_{p} are positively proportional.

Consequently, when the direction of Lorentz force acting on the fluid is upward the sinking velocity of the particle will be increased, during the continuous powder injecting process the particles are easier sunk into the lower region of the melt pool, and the particles will be trapped in the upper region when the direction of Lorentz force acting on the fluid is downward.

The exact trapped positions of particles are described by the simulation model. The particle distributions in the longitudinal sections of the LMI-layers are shown in Figure 8, *a*, *b*. The dots represent the injected particles, the orientation of tails indicates the motion direction of particles, and the length of tails indicates the magnitude of motion velocity of particles. With the same LMI process parameters, the number of injected particles, depth of melt pool and solidification duration are all the same. During the continuous LMI process, the particles are homogeneously distributed in the melt pool (see Figure 8, *b*). Sinking velocity of particles is damped with the effect of downward Lorentz force (see Figure 8, *a*).

Within the same solidification time, the particles injected into the melt pool can hardly be sunken to the bottom of melt pool before its solidification, and they

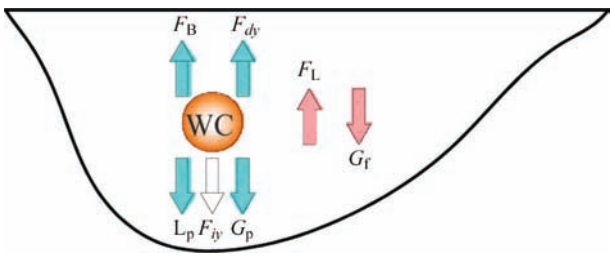

Figure 7. Diagram of forces acting on the particle and surrounding fluid

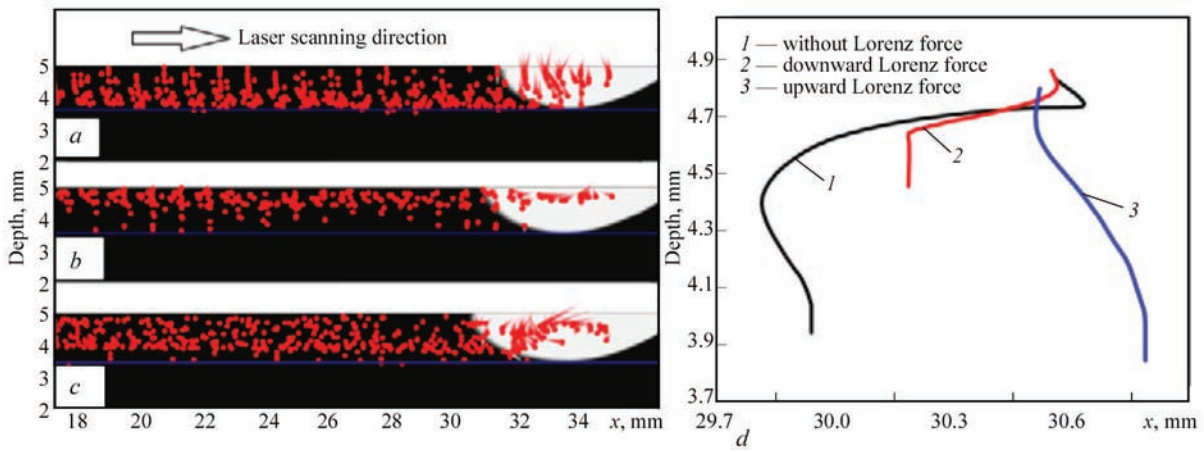

Figure 8. Simulated trapped position of particles in LMI-layer with upward (*a*) and downward (*b*) Lorentz force and without it (*c*), and sinking trajectories of injected particles (*d*)

are concentrated in the upper region of melt pool. In fact, the particles in the melt pool are not sunken along the straight line. The sinking trajectories were calculated by the simulation model (Figure 8, *d*). (Note that the sinking trajectories are different for the particles in different injected positions, the particles shown in Figure 8, *c* are taken from the central zone of the laser spot.). When the particles penetrate the surface of the melt pool, they are transmitted along with the fluid motion due to the strong Marangoni convection at the surface. The resulted sinking trajectories of particles become different mainly because of the electric-magnetic synergistic effect. The resultant buoyancy acting on the particles is increased with the downward Lorentz force. As a result, the sinking depth of the particles is reduced more obviously. Meanwhile the particles near the surface of the melt pool are influenced more by the Marangoni convection, and they are easier dragged to the edge of the melt pool, where it is prone to solidify.

Equation (18) is obtained from (16) through expanding the forces F_B and L_p. The equivalent gravity acceleration is assumed to be the synthesis of local gravity acceleration and Lorentz force related to the density of fluid. According to the above equations, when the Lorentz force and gravity force are in the same direction, the particles in the melt pool are just in hypergravity state, while when the Lorentz force and gravity force are in the opposite direction, the particles in the melt pool can be regarded in hypogravity state. In summary, the direction of the Lorentz force can be easily adjusted by changing the directions of electric and magnetic fields, thus to control the movement of the reinforcement particles in LMI process:

$$\left(g - \frac{jB}{\rho_f}\right)\rho_f V + F_{dy} - G_p + F_{iy} = 0, \qquad (20)$$

where g is the local acceleration of gravity.

Conclusions

The electric-magnetic synergistic effect on the reinforcement particle distribution in LMI was studied experimentally and using simulation. The Lorentz force induced by EMCF can change the gradient distribution of WC particles. Their distributions in the LMI-layers were influenced by EMCF without adjusting the original LMI parameters. When the Lorentz force and gravity force are in the same direction, the majority of particles are trapped in the upper region, while when the Lorentz force and gravity force are in the opposite direction, most particles are concentrated in the lower region. With the assistance of EMCF the sinking velocity and trajectory of WC particles were changed due to the additional volume force acted on the fluid of melt pool during LMI process.

Acknowledgements. *The authors are grateful for financial supports from the National Natural Science Foundation of China (51475429). The authors also would like to specially appreciate Prof. Rong Liu from Carleton University for her kind help in article modification.*

1. Liu, D., Chen, Y., Li, L. et al. (2008) In situ investigation of fracture behavior in monocrystalline WCp-reinforced Ti–6Al–4V metal matrix composites produced by laser melt injection. *Scripta Materialia,* **59**, 91–94.
2. Li, L., Liu, D., Chen, Y. et al. (2009) Electron microscopy study of reaction layers between single-crystal WC particle and Ti–6Al–4V after laser melt injection. *Acta Materialia*, **57**, 3606–3614.
3. Verezub, O., Kálazi, Z., Sytcheva, A. et al. (2011) Performance of a cutting tool made of steel matrix surface nano-composite produced by in situ laser melt injection technology. *J. Materials Proc. Techn.*, **211**, 750–758.
4. Do Nascimento, A.M., Ocelík, V., Ierardi, M.C.F. et al. (2008) Wear resistance of WCp/duplex stainless steel metal matrix composite layers prepared by laser melt injection. *Surface and Coatings Techn.*, **202**, 4758–4765.

5. Cabeza, M., Castro, G., Merino, P. et al. (2014) A study of laser melt injection of TiN particles to repair maraging tool steels. *Surface and Interface Analysis*, **46**, 861–864.
6. Do Nascimento, A.M., Ocelík, V., Ierardi, M.C.F. et al. (2008) Microstructure of reaction zone in WCp/duplex stainless steels matrix composites processing by laser melt injection. *Surface and Coatings Techn*., **202**, 2113–2120.
7. Vreeling, J.A, Ocelík, V., Pei, Y.T. et al. (2000) Laser melt injection in aluminum alloys: On the role of the oxide skin. *Acta Materialia*, **48**, 4225–4233.
8. Li, F.Q., Li, L.Q., Chen, Y.B. (2013) Arc enhanced laser melt injection of WC particles on Al surface. *Surface Eng.*, **29**, 296–299.
9. Pei, Y.T., Ocelik, V., de Hosson, J.T.M. (2002) SiCp/Ti6Al4V functionally graded materials produced by laser melt injection. *Acta Materialia*, **50**, 2035–2051.
10. Vreeling, J.A., Ocelík, V., de Hosson, J.T.M. (2002) Ti–6Al–4V strengthened by laser melt injection of WCp particles. *Ibid*., **50**, 4913–4924.
11. Chen, Y., Liu, D., Li, F. et al. (2008) WCp/Ti–6Al–4V graded metal matrix composites layer produced by laser melt injection. *Surface and Coatings Techn.*, **202**, 4780–4787.
12. Liu, A., Guo, M., Hu, H. (2009) Improved wear resistance of low carbon steel with plasma melt injection of WC particles. *J. Materials Eng. and Performance*, **19**, 848–851.
13. Liu, A., Guo, M., Hu, H. et al. (2008) Microstructure of Cr_3C_2-reinforced surface metal matrix composite produced by gas tungsten arc melt injection. *Scripta Materialia*, **59**, 231–234.
14. Guo, M., Liu, A., Zhao, M. et al. (2008) Microstructure and wear resistance of low carbon steel surface strengthened by plasma melt injection of SiC particles. *Surface and Coatings Techn.*, **202**, 4041–4046.
15. Liu, A., Guo, M., Zhao, M. et al. (2007) Microstructures and wear resistance of large WC particles reinforced surface metal matrix composites produced by plasma melt injection. *Ibid*., **201**, 7978–7982.
16. Liu, D., Li, L., Li, F. et al. (2008) WCp/Fe metal matrix composites produced by laser melt injection. *Ibid*., **202**, 1771–1777.
17. Verezub, O., Kálazi, Z., Buza, G. et al. (2009) In-situ synthesis of a carbide reinforced steel matrix surface nanocomposite by laser melt injection technology and subsequent heat treatment. *Ibid*., **203**, 3049–3057.
18. Guo, B., Fletcher, D.F., Langrish, T.A.G. (2004) Simulation of the agglomeration in a spray using Lagrangian particle tracking. *Appl. Math. Modelling*, **28**, 273–290.
19. Minier, J.-P. (2015) On Lagrangian stochastic methods for turbulent polydisperse two-phase reactive flows. *Progress in Energy and Combustion Sci.*, **50**, 1–62.
20. Chen, Y., Liu, D., Li, L. et al. (2009) Microstructure evolution of single crystal WCp reinforced Ti–6Al–4V metal matrix composites produced at different cooling rates. *J. Alloys and Comp.*, **484**,108–112.
21. Kloosterman, A.B., Kooi, B.J., de Hosson, J.T.M. (1998) Electron microscopy of reaction layers between SiC and Ti–6Al–4V after laser embedding. *Acta Materialia*, **46**, 6205–6217.
22. Anandkumar, R., Almeida, A., Vilar, R. et al. (2009) Influence of powder particle injection velocity on the microstructure of Al–12Si/SiCp coatings produced by laser cladding. *Surface and Coatings Techn.*, **204**, 285–290.
23. Gatzen, M., Tang, Z., Vollertsen, F. (2011) Effect of electromagnetic stirring on the element distribution in laser beam welding of aluminium with filler wire. *Physics Procedia*, **12**, 56–65.
24. Tang, Z., Gatzen, M. (2010) Influence on the dilution by laser welding of aluminum with magnetic stirring. *Ibid.*, **5**, 125–137.
25. Gatzen, M. (2012) Influence of low-frequency magnetic fields during laser beam welding of aluminium with filler wire. *Ibid*., **39**, 59–66.
26. Velde, O., Gritzki, R., Grundmann, R. (2001) Numerical investigations of Lorentz force influenced Marangoni convection relevant to aluminum surface alloying. *Int. J. Heat and Mass Transfer*, **44**, 2751–2762.
27. Bachmann, M., Avilov, V., Gumenyuk, A. et al. (2013) About the influence of a steady magnetic field on weld pool dynamics in partial penetration high power laser beam welding of thick aluminium parts. *Ibid*., **60**, 309–321.
28. Schneider, A., Avilov, V., Gumenyuk, A. (2013) Laser beam welding of aluminum alloys under the influence of an electromagnetic field. *Physics Procedia*, **41**, 4–11.
29. Zhou, J., Tsai, H.-L. (2007) Effects of electromagnetic force on melt flow and porosity prevention in pulsed laser keyhole welding. *Int. J. Heat and Mass Transfer*, **50**, 2217–2235.
30. Bachmann, M., Avilov, V., Gumenyuk, A. et al. (2012) Numerical simulation of full-penetration laser beam welding of thick aluminium plates with inductive support. *J. Physics D: Appl. Physics*, **45**, 035201.
31. Akbari, M., Saedodin, S., Toghraie, D. et al. (2014) Experimental and numerical investigation of temperature distribution and melt pool geometry during pulsed laser welding of Ti6Al4V alloy. *Optics & Laser Techn.*, **59**, 52–59.
32. Morville, S., Carin, M., Peyre, P. et al. (2012) 2D longitudinal modeling of heat transfer and fluid flow during multilayered direct laser metal deposition process. *J. Laser Appl.*, **24**, 032008.
33. Brent, A.D., Voller, V.R., Reid, K.J. (1988) Enthalpy-porosity technique for modeling convection-diffusion phase change: Application to the melting of a pure metal. *Numerical Heat Transfer*. Pt B: Fundamentals, **13**, 297–318.
34. Fu, Y., Loredo, A., Martin, B. et al. (2002) A theoretical model for laser and powder particles interaction during laser cladding. *J. Materials Proc. Techn.*, **128**, 106–112.

Received 08.12.2015